



ORIGINAL RESEARCH ARTICLE

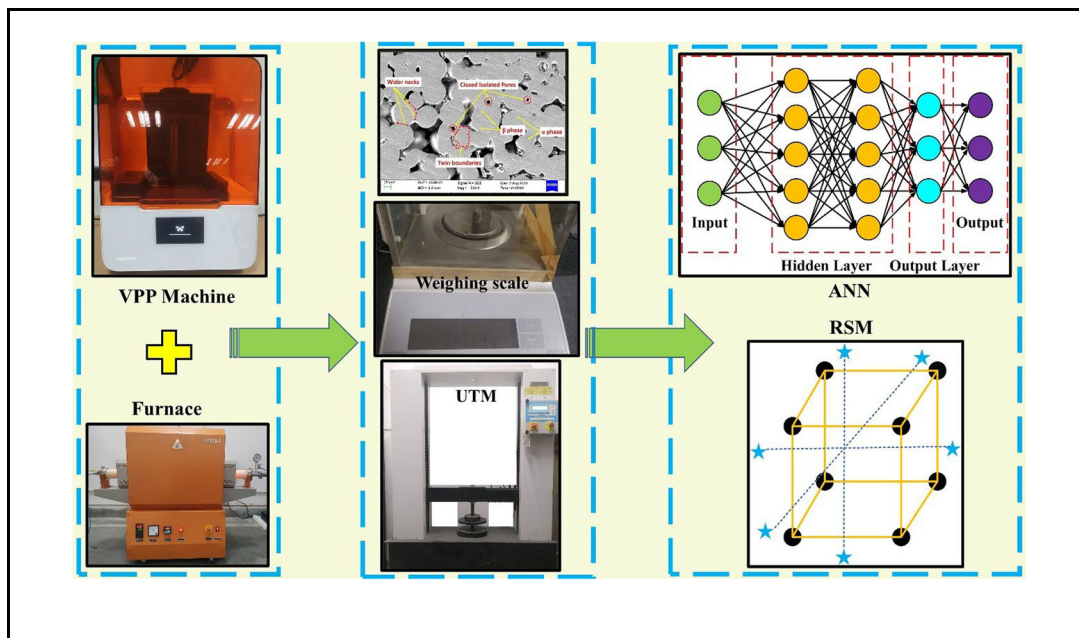
A Comparative Study of Artificial Neural Network and Regression Model for Hybrid Additive Manufacturing of Ti6Al4V Parts and Microstructural Analysis

Garvit Singh, Shailendra Kumar , and Pawan Sharma

Submitted: 24 February 2024 / Revised: 1 May 2024 / Accepted: 1 June 2024

In the present work, a comparative study of artificial neural network (ANN) and regression model for hybrid additive manufacturing (HAM) of Ti6Al4V parts is performed. This study is carried out to identify the best model for the prediction of optimal process parameters. HAM is a fusion of vat photopolymerization (VPP)-based 3D printing and powder metallurgy-based pressureless sintering (PS) technique. Microstructural studies of the fabricated parts are performed using SEM micrographs, and further XRD analysis is used to confirm the phases and their constituents produced during fabrication. To formulate the ANN model, 70% of the datasets are utilized for training, 15% for cross-validation, and the remaining 15% from a total of 20 experimental datasets for testing purposes. A backpropagation training algorithm is used to train and fit the ANN model. Further, a central composite design (CCD)-based regression model is generated to compare it with the ANN model. The findings of predicted values from both regression and the developed ANN model strongly align with experimental outcomes. Moreover, the ANN model demonstrated superior predictive performance, as evidenced by lower mean absolute percentage error (MAPE), mean square error (MSE), and mean absolute error (MAE) values compared to the multiple regression. Additionally, the coefficient of correlation (R) value for ANN model is close to 1, signifying a highly favorable correlation between the experimental and predicted outcomes. Microstructural evaluation reveals a typical Widmanstatten structure with both $\alpha + \beta$ colonies with fine β colonies trapped inside large α grains leading to lamellae structure as observed in SEM micrographs. Moreover, the dimples in the microstructure contribute to the ductile type of fracture, as observed in the failure analysis.

Graphical Abstract



Garvit Singh and Shailendra Kumar, Department of Mechanical Engineering, S.V. National Institute of Technology, Surat, India; and Pawan Sharma, Department of Mechanical Engineering, Indian Institute of Technology-Banaras Hindu University, Varanasi, India. Contact e-mail: skbudhwar@med.svnit.ac.in.

Keywords artificial neural network (ANN), hybrid additive manufacturing (HAM), pressureless sintering, Ti6Al4V, VAT photopolymerization (VPP)

1. Introduction

Ti6Al4V is the premier material in the titanium family, owing to its outstanding features, including a high strength-to-weight ratio, magnificent corrosion resistance, and biocompatibility. (Ref 1-3). These attributes render it well suited for biomedical applications, especially in orthopedic implants, where it replaces missing or damaged hard tissues. (Ref 4). However, the challenge associated with its widespread use is the density mismatch between human bone and Ti alloys (Ref 5). The elastic modulus of human bone ranges from (0.1-30 GPa), whereas Ti alloys vary from (90-110 GPa) (Ref 6). This huge mismatch in elastic modulus gives rise to a severe problem of “stress shielding,” which could culminate in bone resorption and implant loosening over the course of time (Ref 3, 6-8). Therefore, one of the auspicious approaches to address this issue involves creating porous titanium with well-defined porosity characteristics, encompassing considerations such as size, distribution, and interconnectivity of the pores (Ref 8). Hence, additive manufacturing (AM) techniques have the potential to revolutionize the production of porous components by enabling the fabrication of intricate, near-net shape parts with the desired level of porosity. It is characterized by a layer-by-layer manufacturing process that directly transforms computer data models into 3D objects (Ref 9). The primary impediment to the widespread application of titanium alloys is their high procurement and processing costs. Moreover, the inflated expenses tied to AM technologies, such as Powder Bed Fusion (PBF) and Direct Energy Deposition (DED), stem not only from the substantial capital investment but also from the considerable processing costs. These costs arise from the need for higher laser power required to achieve coalescence between powder particles, compounded by Ti alloy’s heightened sensitivity toward oxygen (Ref 3, 8-10). Hence, these challenges have prompted researchers to seek more economically feasible processes for fabricating titanium components encompassing near-net shape powder metallurgy techniques (Ref 10).

Powder metallurgy (PM) techniques, known for their cost-effectiveness, offer a practical solution for fabricating porous Ti6Al4V components, which addresses issues such as high operating cost and stress shielding. Further, when combined with polymer-based 3D printing methods and employed for the production of porous metallic components, it falls within the realm of indirect additive manufacturing (I-AM), as suggested by Mun et al. (Ref 11). Researchers such as Sharma et al. (Ref 12) utilized microwave (MW) technology for the development of pure iron cylindrical specimens by combining powder metallurgy technology, such as pressureless sintering, along with VPP-based 3D printing and called it rapid tooling (RT). Similarly, Singh et al. (Ref 13) produced Ti6Al4V samples using microwave sintering and VPP-based 3D printing. They assessed the most appropriate process variables that yield the lowest pore size and maximum tensile strength. Shahzad et al. (Ref 14) employed Indirect selective laser (I-SLS) sintering to create high-density ceramic components by utilizing unique

powder preparation and post-processing procedures. This technique utilizes an organic polymer that evaporates once exposed to laser irradiation, resulting in coalescence between powder particles. Hoorick et al. (Ref 15) used I-AM to develop a polyester scaffold that served as a temporary (sacrificial) substitute for the hydrogel material during UV cross-linking, avoiding the collapse of the hydrogel structure, which is impossible with conventional AM approach. Furthermore, Mun et al. (Ref 16) proposed and executed a possible substitute process for producing 3D network cellular metals called indirect AM-based casting (I-AM casting), which combines inkjet wax 3D printing with metal casting. Moreover, Wang et al. (Ref 17) used infiltration casting coupled with SLS to create ordered porous aluminum through indirect rapid prototyping.

Based on the literature research, it is noticed that more effort needs to be made by the researchers to create a method for producing near-net shape components with the desired amount of porosity for biological applications. Hence, a novel hybrid additive manufacturing (HAM) approach based on the amalgamation of VPP-based 3D printing and pressureless tube sintering is developed by authors’ research group to address the issue of creating complex, near-net shape components especially for highly reactive materials such as Ti6Al4V. The main objective of the present investigation, is to perform a comparative study between an artificial neural network (ANN) and multiple regression model for hybrid additive manufacturing (HAM) of Ti6Al4V parts. This study will aid to identify the best prediction model for HAM of Ti6Al4V parts, whose outcomes closely align with the experimental values. The subsequent section of paper describes the complete HAM methodology of Ti6Al4V parts. The current study is an extension of previous work of authors’ research group (Ref 18), and design data from that study is utilized to assess the potential of an artificial intelligence (AI) algorithm for anticipating the optimal process parameters for the fabrication of Ti6Al4V parts using HAM.

2. Materials and Methods

The Ti6Al4V spherical powder, as depicted in Figure 1, is used to fabricate cylindrical parts using PS technique. Furthermore, EDX analysis is performed to confirm the presence of chemical elements such as Ti, Al, and V in the desired amount. From the magnified SEM micrograph, it is noticeable that the powder morphology is nearly spherical in nature, whose average particle size (APS) is around 80 μm , as measured by ImageJ software (an open-source software developed by LOCI, University of Wisconsin, USA). The chemical composition of Ti6Al4V powder is given in Table 1.

Spherical powders with a minimal APS were chosen because they demand less activation energy to achieve coalescence during sintering (Ref 19).

In the present work, 20 experimental datasets obtained from the author’s aforementioned prior research are required for developing both the ANN and the multiple regression model.

2.1 Fabrication Methodology

In the HAM methodology, CAD model is created using a 3D modeling software package (SolidWorks v.2015). For the

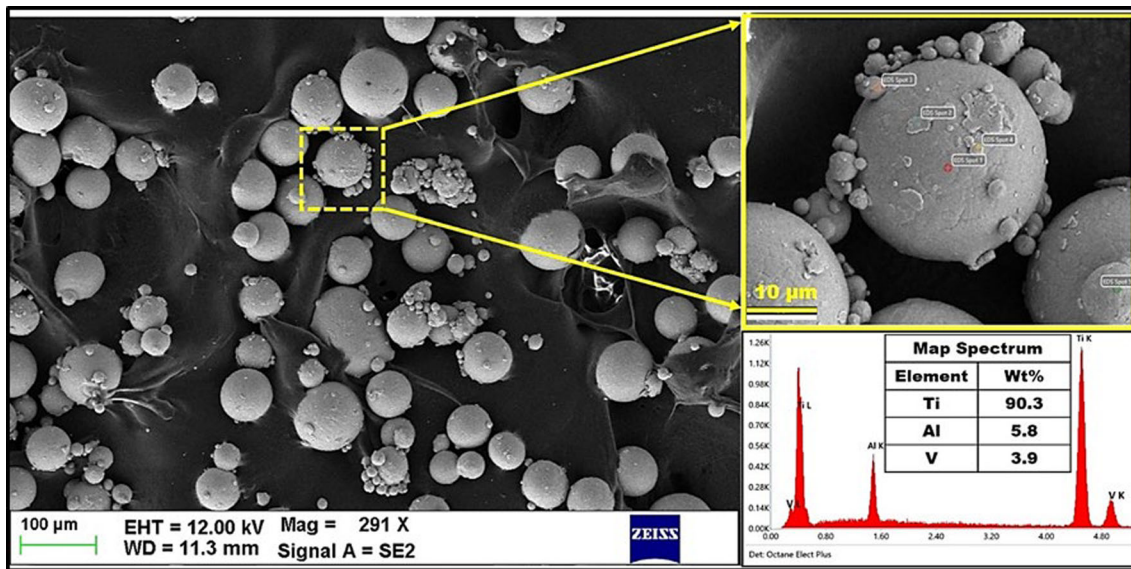


Fig. 1 SEM image of powder morphology with EDX analysis (APS of powder particle – 80 µm)

Table 1 The chemical constituents of Ti6Al4V (As received) powder

Material	Purity	Ti, %	Al, %	V, %	Mg, %	Mn, %	Mo, %
Ti6Al4V	99.90%	89.10	5.70	5.10	0.03	0.01	0.01

study, a cylindrical shape with a height of 15 mm and a diameter of 10 mm was selected. After that, the CAD file is converted into STL file format, which is required for the preform software of VPP-based 3D printing machines (Make: M/s Formlabs 3B + , USA). Further, the necessary support structures and ideal orientation for successful printing of the pattern are performed in the Formlabs software. Once the pattern is printed, it undergoes post-processing that involves dipping in propanol solutions for 15 minutes and is then placed inside the curing furnace at 60°C for 30 minutes. Subsequently, the pattern is encased in a silicon mold, and a mixture of phosphate investment powder and hardener liquid is poured into the mold. Further, the mold housing the pattern is introduced into a furnace and heated to form the cavity as the pattern evaporates.

The cavity created in the mold is then filled with metallic powders under ultrasonic vibrations and finally by tapping at the bottom of the mold. Once the powder is loaded in the mold, it is then placed inside the tube sintering furnace, where a vacuum is created to eliminate any chances of oxide formation due to the presence of contaminants and atmosphere in the tube. After the vacuum is created in the tube for 10-15 minutes, inert gas purging of argon is done while initiating the heater to avoid the formation of oxides during the sintering process. Further, after the completion of the sintering cycle, the fabricated part is taken out and subjected to post-processing. The overall fabrication methodology of HAM is depicted in Figure 2(a).

After the post-processing of the sintered parts, the measurement of responses such as %shrinkage, %porosity, and CYS is performed as shown below.

The bulk porosity is measured using Equation 1 (Ref 12).

$$P = \left(\frac{\rho_s - \rho_a}{\rho_s} \right) \times 100 \quad (\text{Eq 1})$$

where ρ_s is the theoretical density and ρ_a is the apparent density in g/cm^3 of the sintered part. Additionally, to calculate the apparent density of the sintered parts, the dry weight and volume of each sample are taken into consideration. The theoretical density of 4.51 g/cm^3 for Ti was selected to calculate bulk porosity.

The shrinkages in the produced samples were assessed according to the ASTM B610-13 standard. The diameter or height of the sintered specimen can be used to calculate the shrinkage. Additionally, it is recommended to measure the most important dimension in line with the standard guidelines. Therefore, the diameter of the sample was used to quantify shrinkage owing to variations in how the powder was filled into each sample. Equation 2 was utilized to compute the percentage shrinkage (Ref 12).

$$\%S = \frac{D_{st} - D_D}{D_D} \times 100 \quad (\text{Eq 2})$$

D_{st} and D_D denote the diameter (in mm) of the sintered specimen manufactured through powder metallurgy and the diameter of die-cavity, respectively.

Cylindrical samples were subjected to uniaxial compressive tests using a universal testing machine as depicted in Figure 2(b) (Make: M/s EQVIMECH-G-310C) with a 50 kN capacity, operated at a cross-head speed of 1 mm/min, to evaluate their compression properties.

Moreover, microstructural and fractography analysis is performed using scanning electron microscopy (SEM) (Make: M/s Zeiss, Germany). Also, to analyze the elemental composition of sintered sample energy-dispersive x-ray spectroscopy (EDX) (Make: M/s Ametek, USA) is performed.

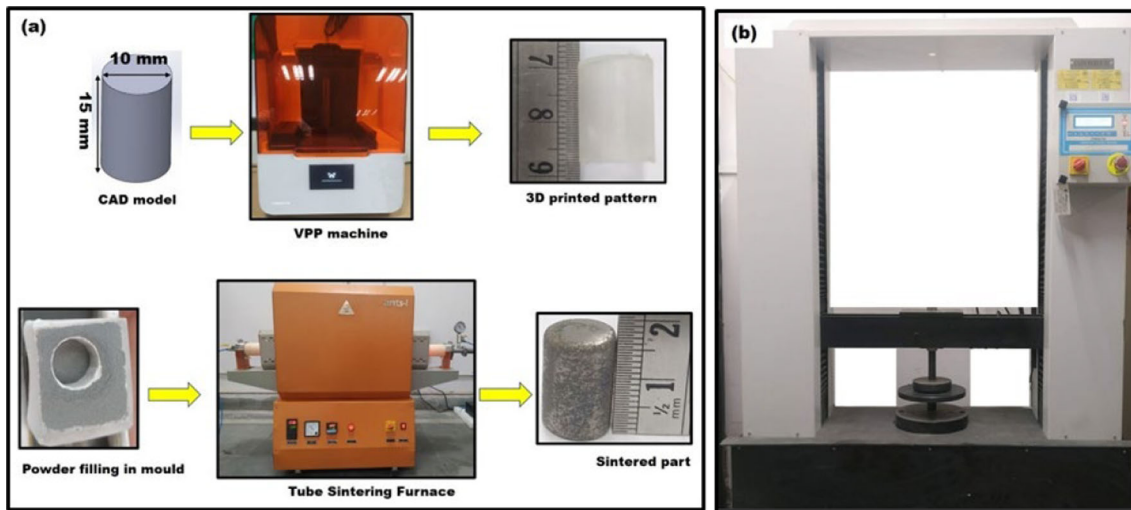


Fig. 2 (a) Fabrication methodology of hybrid additive manufacturing, (b) UTM

Table 2 Experimental results

Run order	Input parameter			Response		
	ST, °C	HT, mins	HR, °C/hr	Shrinkage, %	Porosity, %	Compressive yield strength, MPa
1	1400	180	180	10.40	19.45	321.37
2	1400	120	180	9.30	18.39	330.25
3	1400	120	180	12.50	16.85	339.01
4	1400	120	180	9.16	13.67	346.25
5	1300	150	150	8.58	21.82	347.23
6	1300	90	150	5.25	27.13	292.71
7	1400	60	180	3.80	25.88	302.81
8	1400	120	180	11.30	14.06	341.52
9	1200	120	180	3.91	31.03	221.80
10	1400	120	180	12.50	17.13	336.98
11	1400	120	120	8.53	18.68	328.45
12	1400	120	180	13.50	18.24	334.68
13	1500	90	150	12.66	9.39	371.30
14	1600	120	180	16.66	1.07	414.07
15	1300	90	210	3.20	33.38	257.45
16	1400	120	240	6.66	23.60	341.91
17	1500	150	150	15.83	4.58	398.90
18	1300	150	210	1.16	28.29	234.60
19	1500	90	210	11.61	19.15	326.25
20	1500	150	210	10.68	13.46	348.75

In the present study, CCD was implemented for the experiment, which is known for its precise analysis of responses with minimal trials (Ref 20, 21). The design includes axial and factorial points, enhancing accuracy in modeling nonlinear relationships (Ref 22). The experiment involved five levels for three machine parameters: sintering temperature (ST), holding time (HT), and heating rate (HR). The upper and lower levels for CCD were determined based on the results of trial experiments, taking into account both the productivity and machine constraints of the tubular furnace.

The effects of aforementioned process parameters have been studied using performance indicators such as %shrinkage, %porosity, and CYS. The ANN and regression models in the current study were developed using the previously tested data of our research group and are given in Table 2.

2.2 Development of ANN Architecture

Artificial neural networks (ANNs) represent a soft computing technique that excels in effectively handling input and output parameters with nonlinear relationships (Ref 23).

It is a computational framework that draws inspiration from the biological brain's structure, processing methods, and learning capabilities. The data that pass through the network impact the configuration of the ANN as the neural network adapts and learns from this input and output information. A distinguishing feature of ANNs is their ability to learn and conclude from past experiences and examples, subsequently allowing them to adjust to evolving circumstances (Ref [24,25]). ANN offers advantages in handling nonlinear relationships, adapting to diverse datasets, and robustness to noise. Further,

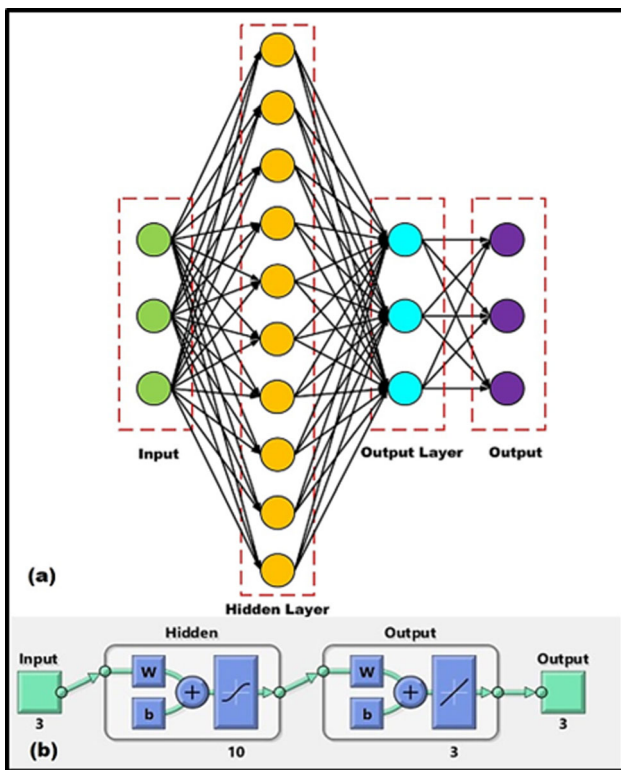


Fig. 3 (a) The complete architecture of ANN scheme (b) ANN block diagram

backpropagation forms the core of neural network training, encompassing the process of disseminating the error rate from forward propagation and transmitting this loss backward through the layers of the neural network to refine and tweak the weights.

The implementation of the ANN was accomplished using the ANN toolbox within MATLAB 2014a software. A feed-forward neural network utilizing the backpropagation training method was employed to construct the ANN model. The accuracy of the ANN model is significantly influenced by the quality and quantity of the dataset used for its training and validation (Ref 26, 27). The architecture of the present ANN model is such that it comprises three inputs and outputs, ten hidden layers, and three output layers. The optimal ANN architecture 3-10-3-3 allows for a flexible representation of the relationships between input and output variables. Also, 10 hidden layer neurons provide sufficient capacity to capture complex patterns in the data while avoiding overfitting, as depicted in Figure 3. Adjustments to the network training parameters were made to achieve the optimal structure with minimal error response. The selected architecture strikes a balance between computational efficiency and model performance avoiding overtraining and overfitting of the model. Subsequently, the training process was validated using the testing set data. Moreover, A (CCD)-based response surface model is formulated, yielding 20 experiments having input and output datasets as shown in Table 3. Among these 20 experiments, the ANN algorithm automatically splits 70% of the datasets for training, 15% for cross-validation, and the remaining 15% for testing purposes, which accounts for 14 samples for training, three samples each for validation and testing, respectively. The allocation of datasets for training,

validation, and testing is carried out through a random selection process. Additionally, the ANN algorithm can autonomously initialize weights and biases based on the dataset's complexity.

Three interlinked layers constitute an ANN; input neurons comprise the first layer. The second layer (hidden) relays data from these neurons and then sends the output neurons to the third layer. The activation of hidden layer neurons employs the "tansig" transfer function, while the "purlin" transfer function is utilized to activate neurons in the outer layer. The Tansig and Purlin functions were calculated using Equations 3 and 4, respectively (Ref 23).

$$\text{tansig}(x) = \frac{2}{1 + e^{-2x}} - 1 \quad (\text{Eq 3})$$

$$\text{purlin}(x) = x \quad (\text{Eq 4})$$

where x represents the input passed to the transfer function.

In the present work, the ANN model was trained using the Levenberg–Marquardt (trainlm function) backpropagation algorithm, which iteratively adjusts weights and biases until achieving an acceptable mean squared error (MSE) as per Equation 5 (Ref 24). Trainlm is the first choice for ANN training due to its speed and reliability. Training entails a continuous process of refining the connection weights until the network produces outputs that closely match the actual experimental values.

$$\text{MSE} = \frac{1}{n} \sum_{i=1}^n (\text{Target value}_i - \text{Predicted value}_i)^2 \quad (\text{Eq 5})$$

where Target value_i is the actual experimental value as obtained from experiment, Predicted value_i is the predicted value, and n is the number of data.

Also, the trial-and-error approach was employed to determine the number of neurons in the hidden layer, aiming to identify an ANN architecture with the lowest MSE across training, validation, and testing datasets.

Figure 4 suggests that a high-performing network with strong predictive capabilities can be developed within a maximum of sixteen iterations (16 epochs). Moreover, the error in the network response was assessed by comparing the expected (predicted) result with the actual experimental result. Also, how well predictions matched the actual results is determined by mean absolute percentage error (MAPE) and is measured as per Equation 6 (Ref 25),

$$\text{MAPE} = \frac{100}{n} \times \sum_{i=1}^n \left| \frac{\text{Target value}_i - \text{Predicted value}_i}{\text{Predicted value}_i} \right| \quad (\text{Eq 6})$$

whereas the mean absolute error (MAE) was assessed by summing the absolute differences between the actual and calculated values for each observation across the entire dataset, and then dividing this sum by the total number of observations in the dataset as depicted in Equation 7 (Ref [27]) .

$$\text{MAE} = \frac{1}{n} \sum_{i=1}^n |\text{Target value}_i - \text{Predicted value}_i| \quad (\text{Eq 7})$$

Further, the results of ANN model are validated, as illustrated in Figure 5. During network training, validation, and testing, the coefficient of correlation (R) tends to

Table 3 Estimated values utilizing ANNs and regression model

S. no.	Experimental results			ANN model			Regression model		
	Sh%	Po%	CYS	Sh%	Po%	CYS	Sh%	Po %	CYS
1	10.40	19.45	321.37	10.24	19.39	321.26	8.14	19.64	324.89
2	9.30	18.39	330.25	11.22	17.02	335.55	10.46	16.79	337.39
3	12.50	16.85	339.01	11.22	17.02	335.55	10.46	16.79	337.39
4	9.16	13.67	346.25	11.22	17.02	335.55	10.46	16.79	337.39
5	8.58	21.82	347.23	8.49	21.83	346.96	8.28	24.19	316.03
6	5.25	27.13	292.71	4.78	29.55	293.40	4.03	27.38	285.16
7	3.80	25.88	302.81	3.77	25.75	302.92	3.88	26.39	295.16
8	11.30	14.06	341.52	11.22	17.02	335.55	10.46	16.79	337.39
9	3.91	31.03	221.80	2.89	30.93	221.96	2.17	32.13	228.67
10	12.50	17.13	336.98	11.22	17.02	335.55	10.46	16.79	337.39
11	8.53	18.68	328.45	8.67	18.81	328.47	8.93	16.76	360.14
12	13.50	18.24	334.68	11.22	17.02	335.55	10.46	16.79	337.39
13	12.66	9.39	371.30	12.58	9.33	371.24	9.98	12.25	354.58
14	16.66	1.07	414.07	16.66	1.07	414.06	16.19	3.04	403.07
15	3.20	33.38	257.45	4.15	33.40	257.78	3.15	28.25	265.58
16	6.66	23.60	341.91	6.15	23.49	341.24	4.08	26.23	306.09
17	15.83	4.58	398.90	15.84	4.62	398.90	14.72	5.60	394.67
18	1.16	28.29	234.60	1.82	28.32	234.84	2.67	28.15	255.22
19	11.61	19.15	326.25	11.53	18.95	326.54	10.74	17.76	361.35
20	10.68	13.46	348.75	11.52	13.29	348.82	10.74	14.19	360.21

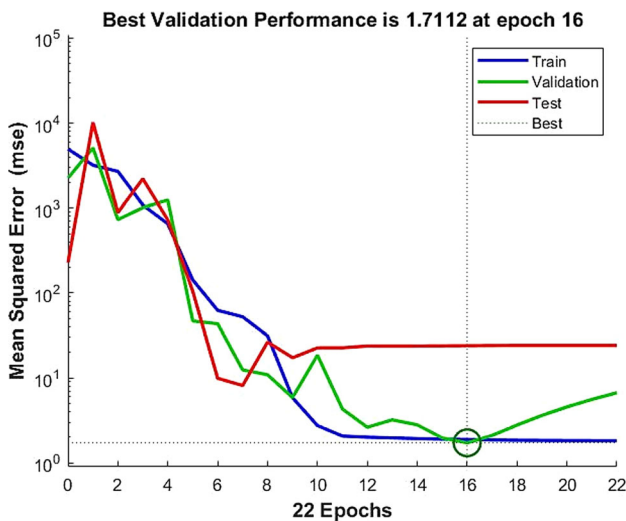


Fig. 4 The training performance graph of ANN

be near the value of one, which elucidates a strong correlation of the model.

2.3 Regression equation

Multiple regression is a statistical approach that explores the relationship between one dependent variable and multiple independent variables. The aim is to use the known values of independent variables to predict the value of the single dependent variable. The goal of this study is to ascertain the extent to which each independent variable contributes to the variance in the dependent variable. The general equation of multiple regression is of the following form:

$$Y = a_0 + a_1X_1 + a_2X_2 + \dots + a_nX_n \tag{Eq 8}$$

In the context, where Y is the dependent variable, X is an independent variable, a0 is the intercept, and a1,...,an are the regression coefficients, these coefficients signify the magnitude and direction of the relationship between each independent variable and the dependent variable. It is an effective approach for predicting the value of the dependent variable using the values of the independent variables. To predict the %shrinkage, %porosity, and CYS, a second-order regression model is developed using design expert software and can be expressed as follows:

$$\begin{aligned} \% \text{ Shrinkage} = & -139.04884 + 0.095339 \times ST + 0.512786 \times HT \\ & + 19.31327 \times HR + 0.000040 \times ST \times HT + 0.008175 \times ST \\ & \times HR - 0.078967 \times HT \times HR - 0.000032 \times ST^2 \\ & - 0.001235 \times HT^2 - 3.95155 \times HR^2 \end{aligned} \tag{Eq 9}$$

$$\begin{aligned} \% \text{ Porosity} = & 284.85711 - 0.163547 \times ST - 0.220997 \times HT \\ & - 62.09651 \times HR - 0.000289 \times ST \times HT + 0.023168 \\ & \times ST \times HR + 0.051384 \times HT \times HR + 0.000020 \times ST^2 \\ & + 0.001730 \times HT^2 + 4.70477 \times HR^2 \end{aligned} \tag{Eq 10}$$

$$\begin{aligned} CYS = & -989.22977 + 1.45507 \times ST + 3.05860 \times HT - 103.32443 \\ & \times HR + 0.000768 \times ST \times HT + 0.131725 \times ST \times HR \\ & - 0.687250 \times HT \times HR - 0.000538 \times ST^2 - 0.007601 \\ & \times HT^2 - 4.27364 \times HR^2 \end{aligned} \tag{Eq 11}$$

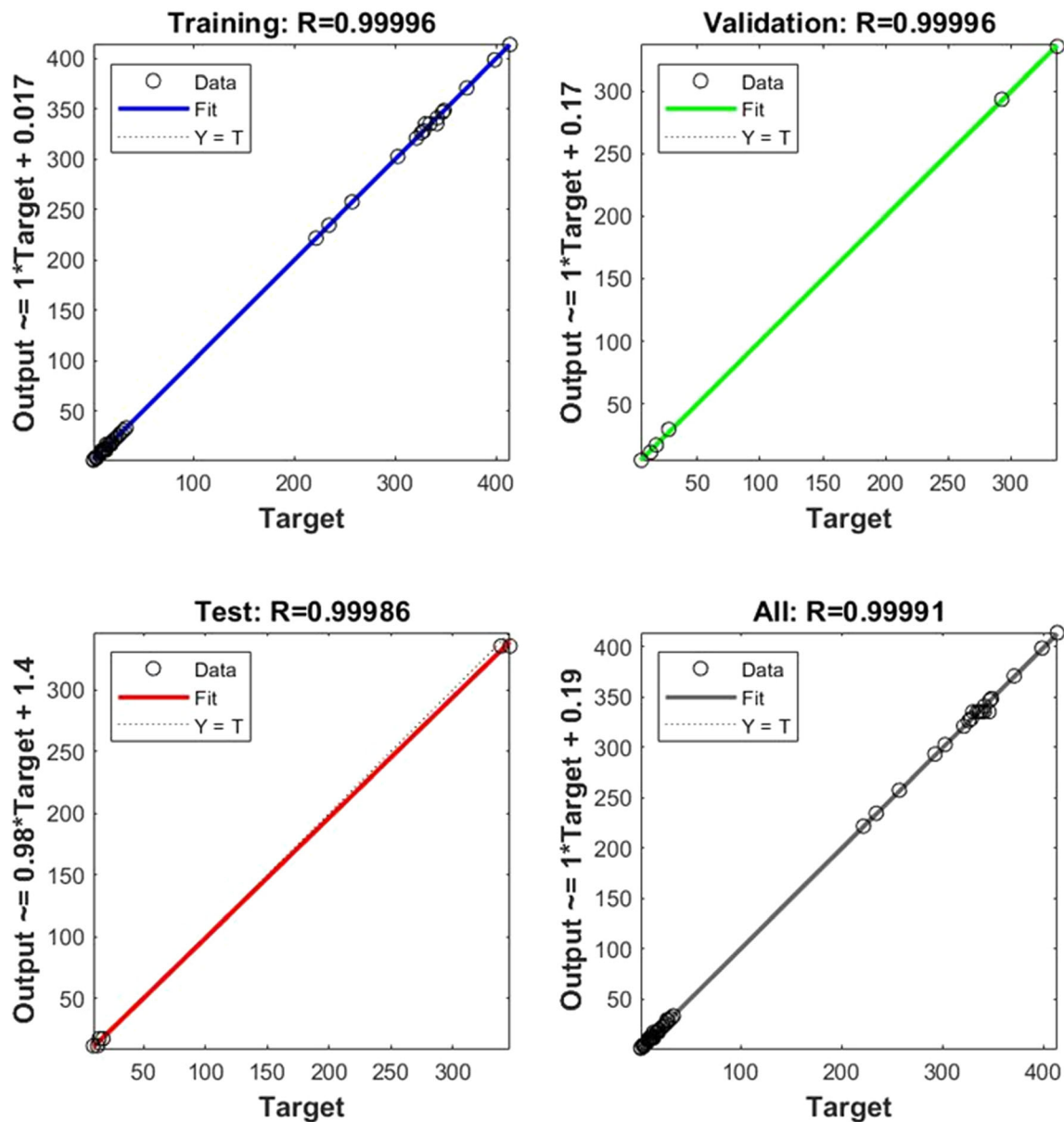


Fig. 5 Validation results of ANN model

3. Results and Discussion

3.1 Microstructural Evolution

Through SEM micrographs, it is evident that during PS, with an increase in temperature, the number of micropores is reduced, whereas the size and number of macropores initially increase and then are reduced, which is attributed to wider necks and layered growth, as depicted in Figure 6. This occurs because activation energy is more readily available at elevated temperatures, facilitating the continuous diffusion and movement of atoms, causing substantial densification during sintering; this finding is in agreement with the findings of Yang et al. (Ref 28). The substantial densification with an increase in temperature during sintering is attributed to the closure of micropores and increased atomic mobility; mass transport results in an increase in shrinkage, as reported by Yang et al. (Ref 28), Sharma et al. (Ref 12). During sintering as the

temperature rises, the diffusion of atoms from the surroundings and the pressure generated by interfacial tension led to the movement of Ti atoms toward the contact point between particles. Consequently, the point contact eventually transforms into the face contact, creates the sintering neck, which keeps growing, and ultimately modifies the shape, size, and number of pores (Ref 28, 29). Further, the EDX analysis confirms the elemental composition of the sintered part and retention of all the main constituents, such as Ti, Al, and V, in the desired amount, as shown in Figure 6(b). Additionally, no oxides of Ti are observed during the sintering process as elucidated by EDX analysis, which ensures good quality of sintering is achieved, similar to the findings of cetinel et al. (Ref 30). Also, both the phases, i.e., α -Ti and β -Ti, are clearly visible in the SEM micrograph as observed in Figure 6(a) and (b), which is also confirmed by the XRD analysis that detects the peaks of both α -Ti and β -Ti phases as revealed in Figure 7.

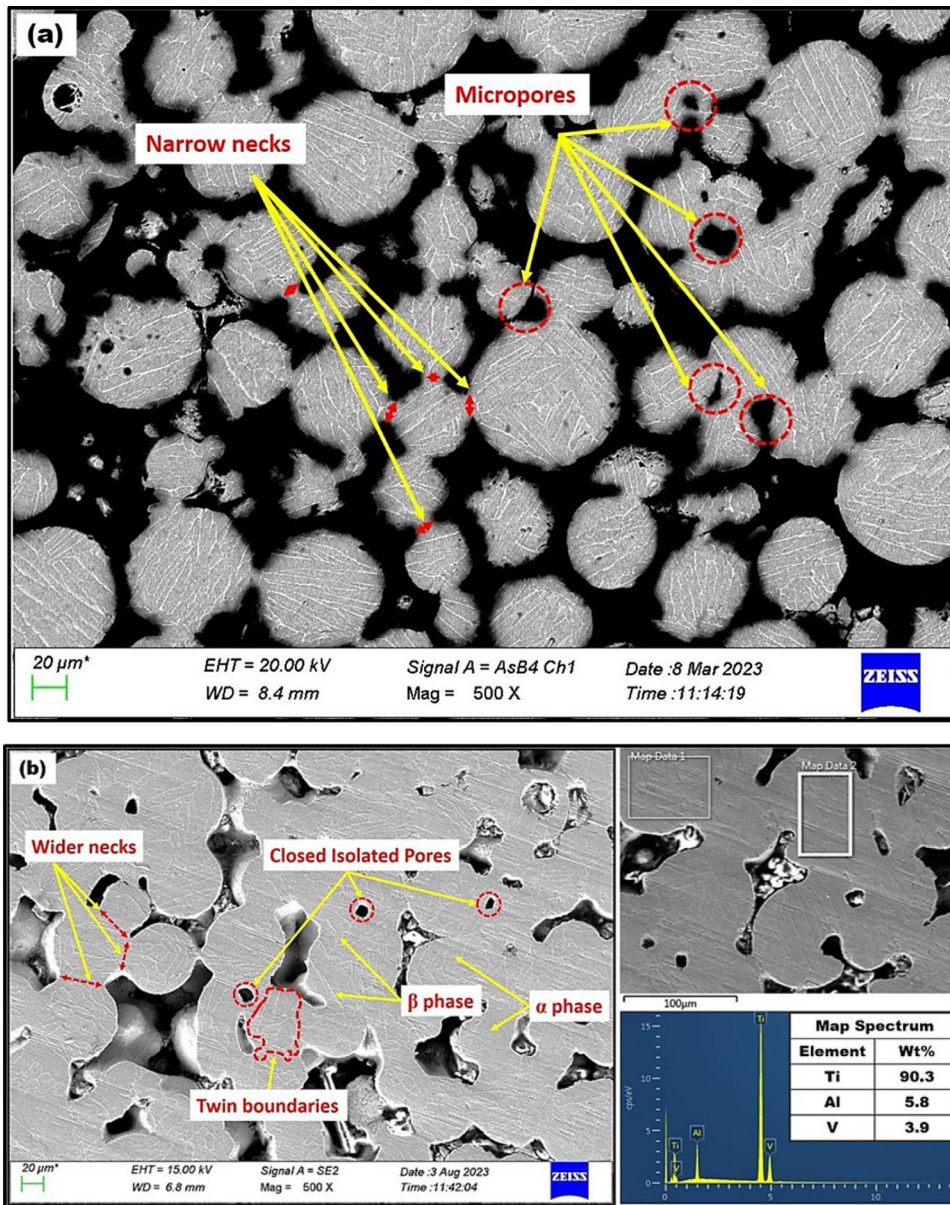


Fig. 6 (a) Microstructural evolution of sample sintered at 1100°C, (b) SEM micrograph of sintered sample at 1400°C with EDX map

In a typical Ti6Al4V alloy, the sintered part may exhibit diverse phases, including lamellae, bimodal, and equiaxed microstructures composed of α , α' , ω , β , and α_2 phases depending upon the sintering temperature range and rate of cooling it undergoes during the process (Ref 31). As in the present study, the sintering temperature range is from 1200°C – 1600°C and the cooling rate chosen to attain room temperature is as low as 180°C/hr. Therefore, at elevated temperatures, the only stable phase that develops is the body-centered cubic (bcc) structure β -Ti phase. Upon gradual cooling, this phase transforms into α -Ti, leading to a structure comprising both α -Ti and β -Ti phases. In Ti6Al4V, aluminum is an α -Ti phase stabilizer, whereas vanadium is a β -Ti phase stabilizer. And from Figure 6, it is visible that the α -phase is represented by the dark areas, which are vanadium-depleted, while the β -phase is represented by the light regions similar to the findings of Esen et al. (Ref 3). Furthermore, it is elucidated from SEM micrographs (Figure 6) that as β -Ti is stable only at higher

temperatures, it is expected to have very low volume fraction in $\alpha + \beta$ microstructure; hence, it is trapped inside large α grains leading to a lamellar type Widmanstatten structure.

3.2 Fractography Analysis

The failure experienced by the porous samples is characterized by the emergence of shear bands at a 45° angle to the compression axis. This occurred due to the detachment of contact zones (necks) between particles, as clearly depicted in Figure 8(a). By brief examination of microstructure using SEM micrograph of fractured sample, it is concurred that instead of complete separation of bonded region, the contact area between powder particles increased and undergoes substantial deformation over the neck region similar to the findings of Esen et al. (Ref 3). Which manifests ductile type of failure of all samples due to the presence of dimples in the microstructure as illustrated in Figure 8(a). Unlike cleavage fracture which falls

in the category of brittle fracture, in all ductile form of fracture, failure initiates with the neck tearing and forming dimples in the test specimen. Fracture initiates with the initiation of cracks that develops along the shear bands at 45° to the axis of load application similar to the findings of Guden et al.(Ref 32). Localization of deformation along the shear bands led to the reduction of load carrying capacity of the deformed sample. Which eventually results in the complete failure of the sample, commencing at the cylindrical sample's corners due to the

dissociation of bonded particles on the shear bands. Furthermore, the failure of interparticle bond area is of ductile nature which consists of dimples. Also, during deformation, initially, non-contacting particles come into contact with nearby particles, inducing inelastic deformation and consequently increasing the contact area between the interacting particles within the interparticle bond region as depicted in Figure 8(a). Due to the accumulation and propagation of voids, macro cracks develop, ultimately resulting in the complete separation of the interparticle bond region, exhibiting a ductile dimple-type failure frequently witnessed in Ti6Al4V alloys under compressive loading.

3.3 Evaluation of Performance of ANN & Regression Model

The accuracy of both the ANN and multiple regression prediction models was assessed through metrics such as the MAPE, MSE, and MAE.

Percentage error estimation of ANN and regression model is presented in Table 4. It is found that the % variation between target value (actual experimental value) and predicted value in regression model is much higher than the ANN model, which confirms the accuracy in prediction of results by ANN is better than any other regression model.

Table 5 depicts the comparative study of performance criteria used for ANN and regression model. Therefore, relying on performance criteria as outlined in Table 5, it is confirmed that ANN demonstrates greater accuracy and outperforms multiple regression model on all responses (%Sh, %Po, and CYS). Additionally, it is found that the ANN model is more

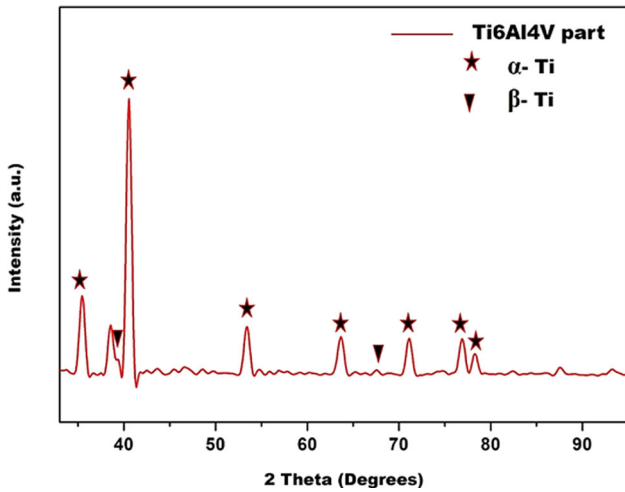


Fig. 7 XRD patterns of sintered part at 1400°C

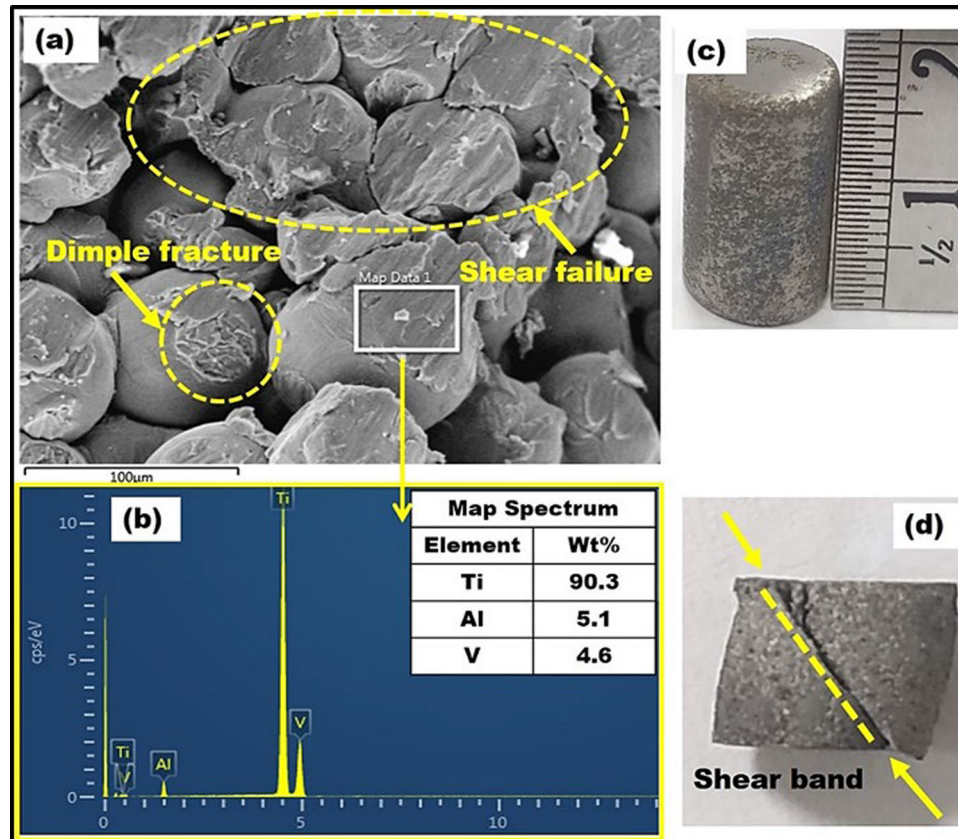


Fig. 8 (a) SEM image of the fractured sample, (b) EDX analysis of the marked region, (c) As-sintered un-fractured sample, (d) fractured sample

Table 4 Percentage error estimation using ANN and regression model

S. No.	ANN (% error)			Regression (% error)		
	Sh%	Po%	CYS	Sh%	Po%	CYS
1	1.51	0.30	0.03	21.71	- 1.01	- 1.10
2	- 20.60	7.43	- 1.60	- 12.46	8.70	- 2.16
3	10.28	- 1.01	1.02	16.33	0.37	0.48
4	- 22.44	- 24.56	3.09	- 14.18	- 22.86	2.56
5	1.08	- 0.04	0.08	3.48	- 10.88	8.98
6	8.93	- 8.92	- 0.24	23.31	- 0.91	2.58
7	0.82	0.49	- 0.04	- 2.20	- 1.98	2.53
8	0.75	- 21.09	1.75	7.44	- 19.43	1.21
9	26.06	0.33	- 0.07	44.60	- 3.56	- 3.10
10	10.28	0.60	0.43	16.33	1.96	- 0.12
11	- 1.59	- 0.72	- 0.01	- 4.74	10.25	- 9.65
12	16.92	6.68	- 0.26	22.53	7.96	- 0.81
13	0.66	0.66	0.02	21.16	- 30.47	4.50
14	0.00	- 0.50	0.00	2.81	- 185.85	2.66
15	- 29.63	- 0.06	- 0.13	1.54	15.37	- 3.16
16	7.65	0.47	0.20	38.74	- 11.14	10.48
17	- 0.07	- 0.97	0.00	7.03	- 22.40	1.06
18	- 57.15	- 0.10	- 0.10	- 130.24	0.49	- 8.79
19	0.73	1.02	- 0.09	7.48	7.27	- 10.76
20	- 7.89	1.23	- 0.02	- 0.57	- 5.46	- 3.28

Table 5 Comparative study of the performance criteria used for ANN and regression model

S.No.	Performance criteria	ANN model			Regression model		
		Sh %	Po %	CYS	Sh %	Po %	CYS
1	MSE	1.00	1.47	9.72	2.48	4.09	293.24
2	MAPE	2.68	1.94	0.20	3.50	13.18	0.29
3	MAE	0.70	0.63	1.54	1.29	1.58	12.82

precise based on the lower values of performance metrics like MAPE, MSE, and MAE in ANN predictions.

4. Conclusion

In the present study, responses, namely shrinkage (Sh %), porosity (Po%) and compressive yield strength (CYS) for HAM of Ti6Al4V parts, are predicted using ANN and multiple regression models by CCD-based experimental datasets. The developed models are evaluated using performance criteria, and their predicted outcomes exhibited strong agreement with the experimental results. The following conclusions are drawn from the present study:

- Percentage error between the experimental values and values predicted by ANN model is minimum as compared to the regression model. The %error estimation predicted by ANN model varies from - 57.15% to 26.06%, - 24.56 to 7.43, - 0.26 to 3.09 for %Sh, %Po, and CYS, respectively.
- Furthermore, for % Sh, %Po, and CYS the values of MSE, MAPE, and MAE using ANN model are 1.00%, 1.47%, and 9.72; 2.68%, 1.94%, and 0.20, 0.70%, 0.63%, and 1.54, respectively.
- SEM micrographs reveal typical Widmanstatten structure containing both $\alpha + \beta$ colonies, fine β colonies trapped inside large α grains leading to lamellae structure. The EDX and XRD results confirm the retention of main constituents such as Ti, Al, and V in the sintered part with α & β phases in the desired level.
- Failure analysis manifests ductile type of failure which is attributed to the presence of dimples in the microstructure. The separation of bonded particles results in increase in area of contacted region which incurs substantial deformation of sintered part leading to dimple fracture and hence ductile failure of the part.

The novelty of this work stems from comparative analysis between artificial neural network (ANN) and multiple regression model for the HAM of Ti6Al4V parts. Furthermore, the approach for algorithm selection, optimization of network architecture, and domain-specific application play a crucial role in identifying the most effective model for predicting optimal process parameters for fabricating Ti6Al4V parts using HAM. Also, the findings of present study will aid in the development of intricate near-net shape objects that are difficult to produce through conventional powder metallurgical processes.

Authors Contribution

G. Singh was involved in writing—original draft, investigation, visualization, and conceptualization. S. Kumar contributed to the conceptualization, supervision, and writing—review and editing. P. Sharma participated in the supervision and writing—review and editing.

Funding

The author(s) did not receive any specific grant from funding agencies in the public, commercial, or not-for-profit sectors for the research, authorship, and/or publication of this article.

Conflict of interest

There is no potential conflict of interest between author(s) with respect to research, authorship, and/or publication of this article.

References

1. V.M. Solorio, H.J. Vergara-Hernández, L. Olmos, D. Bouvard, J. Chávez, O. Jimenez, and N. Camacho, Effect of the Ag Addition on the Compressibility, Sintering and Properties of Ti6Al4V/XAg Composites Processed by Powder Metallurgy, *J. Alloys Compd.*, 2022, **890**, p 161813. <https://doi.org/10.1016/j.jallcom.2021.161813>
2. Z. Li, M. Chuzenji, and M. Mizutani, Compression and Fatigue Performance of Ti6Al4V Materials with Different Uniform and Gradient Porous Structures, *Mater. Sci. Eng. A*, 2023, **873**, p 145030. <https://doi.org/10.1016/j.msea.2023.145030>
3. Z. Esen, E. TarhanBor, and Ş Bor, Characterization of Loose Powder Sintered Porous Titanium and Ti6Al4V Alloy, *Turkish J. Eng. Environ. Sci.*, 2009, **33**(3), p 207–219.
4. M. Nasser Alhaji, Z. Ariffin, Z. Ab-Ghani, Y. Johari, Y. Naito, and M. Jaafar, A Novel Moldless Porous Titanium Formulae for Dental Post System: Part 1—Development and Characterization, *Mater. Today Proc.*, 2022, **66**, p 2670–2675. <https://doi.org/10.1016/j.matpr.2022.06.492>
5. J.P. Li, P. Habibovic, M. van den Doel, C.E. Wilson, J.R. de Wijn, C.A. van Blitterswijk, and K. de Groot, Bone Ingrowth in Porous Titanium Implants Produced by 3D Fiber Deposition, *Biomaterials*, 2007, **28**(18), p 2810–2820.
6. H.-C. Hsu, S.-K. Hsu, S.-C. Wu, P.-H. Wang, and W.-F. Ho, Design and Characterization of Highly Porous Titanium Foams with Bioactive Surface Sintering in Air, *J. Alloys Compd.*, 2013, **575**, p 326–332. <https://doi.org/10.1016/j.jallcom.2013.05.186>
7. G. Gagg, E. Ghassemieh, and F.E. Wiria, Effects of Sintering Temperature on Morphology and Mechanical Characteristics of 3D Printed Porous Titanium Used as Dental Implant, *Mater. Sci. Eng. C*, 2013, **33**(7), p 3858–3864. <https://doi.org/10.1016/j.msec.2013.05.021>
8. S.W. Kim, H. Do Jung, M.H. Kang, H.E. Kim, Y.H. Koh, and Y. Estrin, Fabrication of Porous Titanium Scaffold with Controlled Porous Structure and Net-Shape Using Magnesium as Spacer, *Mater. Sci. Eng. C*, 2013, **33**(5), p 2808–2815. <https://doi.org/10.1016/j.msec.2013.03.011>
9. F.E. Wiria, S. Maleksaedi, and Z. He, Manufacturing and Characterization of Porous Titanium Components, *Prog. Cryst. Growth Charact. Mater.*, 2014, **60**(3–4), p 94–98. <https://doi.org/10.1016/j.pcrysgrow.2014.09.001>
10. F.H. Froes and B. Dutta, The Additive Manufacturing (AM) of Titanium Alloys, *Adv. Mater. Res.*, 2014, **1019**, p 19–25.
11. J. Mun, J. Ju, and J. Thurman, Indirect Additive Manufacturing of a Cubic Lattice Structure with a Copper Alloy, in *2014 Int. Solid Free. Fabr. Symp.* p 665–687 (2014)
12. P. Sharma and P.M. Pandey, Rapid Manufacturing of Biodegradable Pure Iron Scaffold Using Amalgamation of Three-Dimensional Printing and Pressureless Microwave Sintering, *Proc. Inst. Mechan. Eng. Part C J. Mechan. Eng. Sci.*, 2019, **233**(6), p 1876–1895. <https://doi.org/10.1177/0954406218778304>
13. D. Singh, A. Rana, P. Sharma, P.M. Pandey, and D. Kalyanasundaram, Microwave Sintering of Ti6Al4V: Optimization of Processing Parameters for Maximal Tensile Strength and Minimal Pore Size, *Metals (Basel)*, 2018, **8**(12), p 1086.
14. K. Shahzad, J. Deckers, J.-P. Kruth, and J. Vleugels, Additive Manufacturing of Alumina Parts by Indirect Selective Laser Sintering and Post Processing, *J. Mater. Process. Technol.*, 2013, **213**(9), p 1484–1494. <https://doi.org/10.1016/j.jmatprotec.2013.03.014>
15. J. Van Hoorick, H. Declercq, A. De Muynck, A. Houben, L. Van Hoorebeke, R. Cornelissen, J. Van Erps, H. Thienpont, P. Dubruel, and S. Van Vlierberghe, Indirect Additive Manufacturing as an Elegant Tool for the Production of Self-Supporting Low Density Gelatin Scaffolds, *J. Mater. Sci. Mater. Med.*, 2015, **26**(10), p 5566.
16. J. Mun, B.-G. Yun, J. Ju, and B.-M. Chang, Indirect Additive Manufacturing Based Casting of a Periodic 3D Cellular Metal-Flow Simulation of Molten Aluminum Alloy, *J. Manuf. Process, Soc. Manuf. Eng.*, 2015, **17**, p 28–40. <https://doi.org/10.1016/j.jmapro.2014.11.001>
17. H. Wang, Y. Fu, M. Su, and H. Hao, A Novel Method of Indirect Rapid Prototyping to Fabricate the Ordered Porous Aluminum with Controllable Dimension Variation and Their Properties, *J. Mater. Process. Technol.*, 2019, **266**(2), p 373–380. <https://doi.org/10.1016/j.jmatprotec.2018.11.017>
18. G. Singh, S. Kumar, and P. Sharma, A Novel Hybrid Additive Manufacturing Methodology for the Development of Ti6Al4V Parts, *J. Mater. Eng. Perform.*, 2023 <https://doi.org/10.1007/s11665-023-08883-5>
19. Z.Z. Fang, “Sintering of Advanced Materials,” *Sintering of Advanced Materials*, Z.Z. Fang, Ed., Copyright © 2010 Woodhead Publishing Limited. All rights reserved., 2010, <https://doi.org/10.1533/9781845699949>
20. R.G. Scott, M.N. Das, and N.C. Giri, Design and Analysis of Experiments, *J. Royal Stat. Soc. Ser. A (Stat. Soc.)*, 1988, **151**(3), p 552. <https://doi.org/10.2307/2983009>
21. N. Bari and S. Kumar, Multi-Stage Single-Point Incremental Forming: An Experimental Investigation of Thinning and Peak Forming Force, *J. Brazilian Soc. Mech. Sci. Eng.*, 2023, **45**(3), p 1–17. <https://doi.org/10.1007/s40430-023-04055-7>
22. J. Sarvaiya and D. Singh, Experimental Investigation of Peak Temperature and Microhardness in Friction Stir Processing of AA6082-T6 Using Taguchi GRA, *Def. Sci. J.*, 2022, **72**(2), p 258–267
23. Jainesh Sarvaiya, and Dinesh Singh, Prediction of Performance Parameters in Friction Stir Processing Using ANN and Multiple Regression Models, *Mater. Today Proc.*, 2023 <https://doi.org/10.1016/j.matpr.2023.04.422>
24. S. Nayak, P. Dhondapure, A.K. Singh, M.J.N.V. Prasad, and K. Narasimhan, Assessment of Constitutive Models to Predict High Temperature Flow Behaviour of Ti-6Al-4V Preform, *Adv. Mater. Proc. Technol.*, 2020, **6**(2), p 244–258. <https://doi.org/10.1080/2374068X.20.1731233>
25. S. Anand Kumar, S.G. Sundara Raman, T.S.N. Sankara Narayanan, and R. Gnanamoorthy, Prediction of Fretting Wear Behavior of Surface Mechanical Attrition Treated Ti-6Al-4V Using Artificial Neural Network, *Mater. Des.*, 2013, **49**, p 992–999. <https://doi.org/10.1016/j.matdes.2013.02.076>
26. M.N. Hajmeer, I.A. Basheer, and Y.M. Najjar, Computational Neural Networks for Predictive Microbiology II. Application to Microbial Growth, *Int. J. Food Microbiol.*, 1997, **34**(1), p 51–66. [https://doi.org/10.1016/S0168-1605\(96\)01169-5](https://doi.org/10.1016/S0168-1605(96)01169-5)
27. A. Costa, G. Buffa, D. Palmeri, G. Pollara, and L. Fratini, Hybrid Prediction-Optimization Approaches for Maximizing Parts Density in SLM of Ti6Al4V Titanium Alloy, *J. Intell. Manuf.*, 2022, **33**(7), p 1967–1989. <https://doi.org/10.1007/s10845-022-01938-9>
28. D. Yang, Z. Tian, J. Song, L. Tengfei, G. Qiu, J. Kang, H. Zhou, H. Mao, and J. Xiao, Influences of Sintering Temperature on Pore Morphology, Porosity, and Mechanical Behavior of Porous Ti, *Mater. Res. Expr.*, 2021, **8**(10), p 106519. <https://doi.org/10.1088/2053-1591/ac1b63>
29. R.M. German, P. Suri, and S.J. Park, Review: Liquid Phase Sintering, *J. Mater. Sci.*, 2009, **44**(1), p 1–39. <https://doi.org/10.1007/s10853-008-3008-0>

30. O. Cetinel, Z. Esen, and B. Yildirim, Fabrication, Morphology Analysis, and Mechanical Properties of Ti Foams Manufactured Using the Space Holder Method for Bone Substitute Materials, *Metals*, 2019, **9**(3), p 340. <https://doi.org/10.3390/met9030340s>
31. Z. Esen and Ş Bor, Characterization of Ti–6Al–4V Alloy Foams Synthesized by Space Holder Technique, *Mater. Sci. Eng. A*, 2011, **528**(7–8), p 3200–3209. <https://doi.org/10.1016/j.msea.2011.01.008>
32. M. Guden, E. Celik, E. Akar, and S. Cetiner, Compression Testing of a Sintered Ti6Al4V Powder Compact for Biomedical Applications, *Mater Charact*, 2005, **54**(4–5), p 399–408.

Publisher's Note Springer Nature remains neutral with regard to jurisdictional claims in published maps and institutional affiliations.

Springer Nature or its licensor (e.g. a society or other partner) holds exclusive rights to this article under a publishing agreement with the author(s) or other rightsholder(s); author self-archiving of the accepted manuscript version of this article is solely governed by the terms of such publishing agreement and applicable law.